Supplementary materials for competing kinetics and He bubble morphology in W

Luis Sandoval,[1] Danny Perez,[1] Blas P. Uberuaga,[2] and Arthur F. Voter[1]

[1] *Theoretical Division, Los Alamos National Laboratory, Los Alamos, NM 87545, USA*
[2] *Materials Science and Technology Division, Los Alamos National Laboratory, Los Alamos, NM 87545 USA*

(Dated: January 23, 2015)

SIMULATION METHODOLOGY

Depth distribution

In a first set of molecular dynamics (MD) simulations, we determined the implantation depth distribution of a single ion impacting the (100) tungsten surface at $T = 1000$ K (see Fig. 1). This has also allowed us to obtain the fraction of reflected particles, and to optimize the size of the simulation box for growth simulations. The incident atom energy was 60 eV, which corresponds to a typical energy expected in ITER [1, 2]. The atoms collided perpendicularly to the tungsten surface at random positions. The depth of the helium atom was registered once it came to a stop in the target, that is, once it reached thermal equilibrium with its surroundings (in about 1 ps of helium-tungsten interaction).

After 4000 impacts (performed independently, not cumulatively) the mean depth of those helium atoms that did not desorb was 10.5 Å. The reflection percentage was 72%, in agreement with recently published results at similar temperatures [3]. The maximum registered depth was ~ 49 Å and no channeling event was observed.

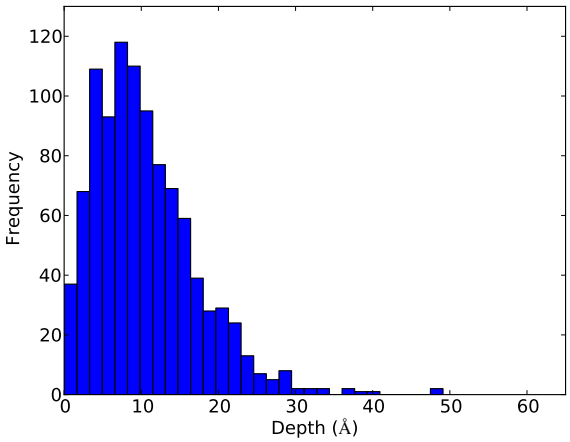

FIG. 1. Histogram for the depth distribution of helium atoms impacting at 60 eV on the (100) surface of tungsten. The depth of the helium atom is registered once the helium atom has come to a stop in the target ($\sim$ 1 ps of helium-tungsten interaction).

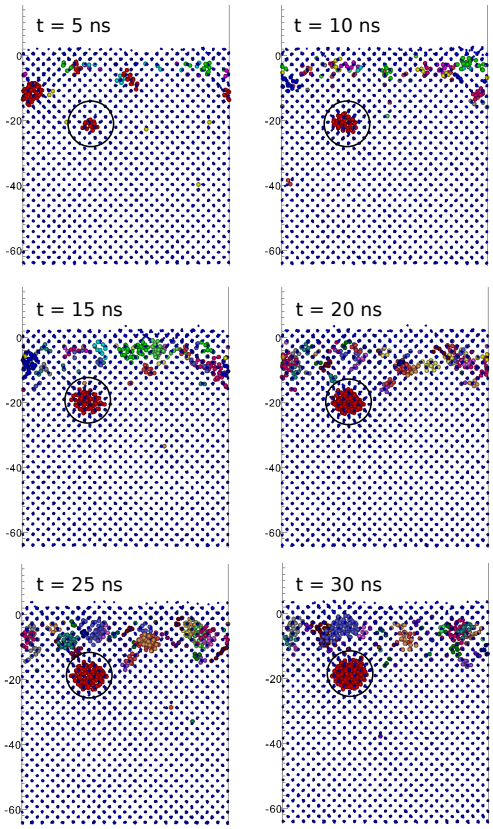

FIG. 2. Snapshots of the implantation process of helium atoms on the (100) surface of tungsten at a rate of 0.2 He ps^{-1}. With a circle we highlight the type of helium bubble of interest in this work. The He atoms are colored according to the cluster they belong to.

Implantation of helium atoms on W(100)

Next, we determined the behaviour of the (100) tungsten surface under a helium flux at $T = 1000$ K, with incident ion energy of 60 eV, using direct MD simulations. The ions again collide perpendicularly to the tungsten surface at random positions, this time cumulatively, with a frequency of 2×10^{11} He s^{-1}, corresponding to a flux of 5×10^{27} He m^{-2} s^{-1}, which is three orders of magnitude higher than that expected in the ITER divertor [4]. Similar simulations have recently been performed by Sefta *et al.* [4]. In Fig. 2 some snapshots from these simulations are shown. Details about the mobility and distribution of clusters have been thoroughly treated by Sefta *et al.* [4]. Our interest in the present work is the

growth process of deep bubbles, such as the one highlighted in Fig. 2, which could reach large sizes (> 100 helium atoms), significantly affecting the morphology of the surface. Over the course of 5000 impacts (25 ns) this bubble acquired 130 helium atoms, which means that ∼ 2.6% of the helium flux contributed to its growth.

Relation between flux and growth rates

To correlate the bubble growth rate and incoming helium flux (at fluxes characteristic of ITER), we ran 100 MD simulations of a system containing a single helium bubble with a radius of 4.8 Å (70 helium atoms) at a depth of 15.9 Å, and a helium atom randomly located in the target, with an initial position weighted according to the depth distribution shown in Fig. 1. The fraction of helium atoms successfully reaching the bubble was 15%. Considering the percentage of impinging helium atoms absorbed by the target (28%, obtained in the depth distribution simulations described above), the resulting fraction of *incoming ions* successfully reaching the bubble is $f = 0.28\frac{15}{100} = 0.042$.

Finally, in order to relate bubble growth rate and the helium flux we have to consider the surface area A

$$\kappa_{\text{growth}} = \phi_{\text{impact}} f A\,, \tag{1}$$

where ϕ_{impact} is the flux of helium atoms, and κ_{growth} denotes the bubble growth rate. Considering the area of our simulation box ($A = 4.05 \times 10^{-17}\,\text{m}^2$), and the helium flux expected at ITER [5] ($\phi_{\text{impact}} \approx 1 \times 10^{24}\,\text{He}\,\text{m}^{-2}\,\text{s}^{-1}$), we obtain $\kappa^{\text{ITER}}_{\text{growth}} = 1.7 \times 10^6\,\text{He}\,\text{s}^{-1}$, which is very close to the slowest growth rate considered in this study ($\kappa_{\text{growth}} = 2 \times 10^6\,\text{He}\,\text{s}^{-1}$).

Dimension of the simulation box

The length of the simulation box perpendicular to the surface was chosen to be ∼ 3.5 times the initial bubble's depth, in order to ensure that the bubble only interacted with the top surface. To choose the box dimensions in the other two directions, we considered an extreme case consisting of a highly pressurized helium bubble close to the bursting point. We examined different simulation-box sizes and characterized the behavior of the atomic strain tensor for the tungsten lattice in minimized configurations. We determined that a size of 20 lattice parameters in each direction was sufficient to avoid significant finite-size effects in the strain field (see Fig. 3). This choice led to a nearly cubic simulation box ($20a \times 20.5a \times 20a$).

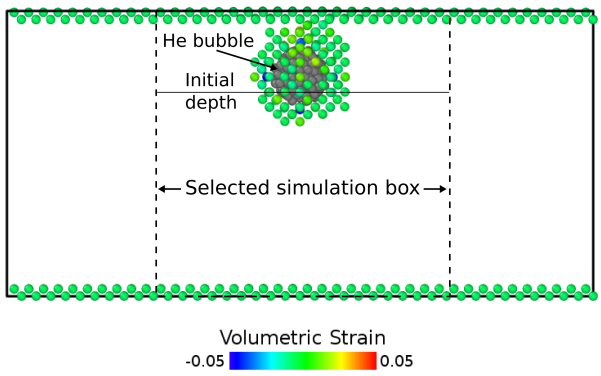

FIG. 3. Selection of the dimensions of the simulation box parallel to the surface. The He bubble is colored in grey, and only W atoms with an absolute volumetric strain larger than 0.005 are shown. The final simulation box side dimensions chosen for our work were about three times the length of the deformed region around the bubble, defined via a threshold volumetric strain value of 0.005.

Insertion of He

In order to avoid nonphysical interaction between the new helium atom and the existing helium atoms, the insertion process was performed as follows: a spherical region with a diameter equal to the tungsten lattice constant was defined around the center of mass of the current helium bubble. A new helium atom was created in this region in such a way that its closest neighbor was located at a distance larger than a minimum threshold value of 0.2 Å. The consideration of the center of mass of the helium bubble is essential, as we do not want to artificially push the bubble in a particular direction. Additionally, the excess kinetic energy caused by the sudden creation of a helium atom in the bubble was rapidly extracted by defining a maximum displacement of 0.1 Å allowed in each MD step, thereby efficiently taking away the excess energy due to the creation of a new He atom. This protocal assumes that bubbles growth occurs through the sequential absorption of single He atoms. It is possible that small clusters of He interstitials would also contribute, but the molecular dynamic simulations of helium implantation have shown that such a contribution is small. At more realistic implantation rates, this effect will be even smaller because of the lower helium interstitial concentration, so this effect was neglected here.

Before the first ParRep simulation block started, the system was equilibrated at 1000 K for 10 ps. Each time a new atom was included in the bubble, another ParRep simulation block was performed with dephasing and correlation times ($\tau_{dephase}, \tau_{corr}$) equal to 10 ps. To avoid biasing against emission of dislocations towards the bottom of the simulation cell, the bottom layers were left free.

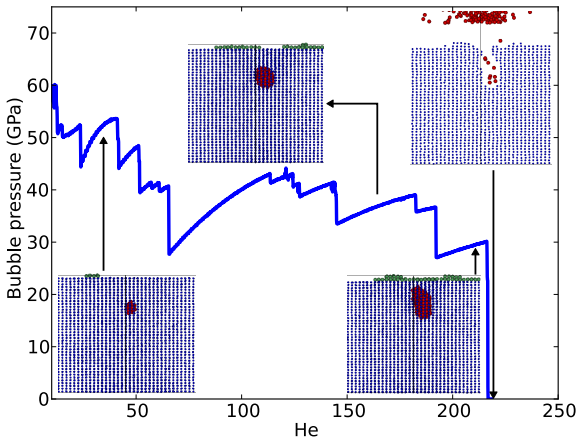

FIG. 4. Evolution of the pressure as a function of the number of He atoms in the bubble for a growth rate of 10^9 He s^{-1}. Corresponding atomistic configurations are reported as insets. W atoms (not including adatoms) are colored in blue, adatoms in green, and He atoms in red.

For all the simulations, we tracked the evolution of the pressure experienced by the helium bubble, as shown in Fig. 4. To do this, we needed the volumetric local stress tensor, which was readily available during MD simulations, and the volume occupied by the helium bubble. The procedure we used to define this volume began by performing a Voronoi tessellation of the complete system, as implemented in LAMMPS using the program voro++ [6]. We took the volume of the helium bubble as the sum of the volumes of the Voronoi cells containing helium atoms. The visualization of atomic configurations was done with VisIt [7] and Ovito [8].

Detection of transitions and point defects

In this work, ParRep transitions are defined as changes in atomic positions where at least one tungsten atom has moved a distance greater than 2.5 Å with respect to a reference configuration that was saved after the previous transition. This check was performed every 1 ps. These transition events basically correspond to the nucleation of Frenkel pairs, diffusion of interstitials, and adatom diffusion. This threshold value of 2.5 Å was obtained by monitoring the atomic displacements associated with jumps in the pressure as a function of time. This value is also lower than $\langle 111 \rangle /2$, the Burgers vector of the prismatic $\langle 111 \rangle$ dislocation loops which eventually form adatom islands once they glide to the surface. We have verified that this catches all transitions. The positions of He atoms are ignored in this check, as the bubble is treated as a single entity, and the helium degrees of freedom evolve much faster than the tungsten degrees of freedom. We never observed the emission of He atoms from the bubble (an event that could be missed by this procedure).

Interstitials and vacancies were detected by using the Wigner-Seitz cell method [9, 10] as implemented in Ovito [8]. In this procedure, atomic configurations are compared with an undisturbed reference configuration. Vacancies are associated with empty Wigner-Seitz cells, and interstitials with Wigner-Seitz cells containing two or more atoms.

ParRep efficiency

The efficiency of the ParRep method is controlled by both the dephasing time ($\tau_{dephase}$), which does not advance the system clock, and the correlation time (τ_{corr}), during which only one processor accumulates simulation time [11]. Using $\tau_{dephase} = \tau_{corr} = 10$ ps, this corresponds to parallel efficiencies of 89% (1 He ns^{-1}, 50 replicas), 82% (0.1 He ns^{-1}, 250 replicas), 71% (0.05 He ns^{-1}, 500 replicas), and 77% (0.002 He ns^{-1}, 10000 replicas). The simulations at a growth rate of 0.002 He ns^{-1} were carried out using $\sim 50\%$ of the cpu computing power of the Titan supercomputer at Oak Ridge National Laboratory. For the fast growth regime, we used a single replica, as parallelization in time was not necessary; this is equivalent to standard MD.

COMMENT REGARDING THE POTENTIAL

We note that many of the simulations that reported using the Juslin and Wirth form of the W-He interaction [4, 12–14] in fact used a slightly different potential than the one given in Juslin and Wirth [15]. Specifically, in the interval [2.7,3.2] Å, the values of the force are lower than those of the published potential, with a maximum difference of 0.16 eV/Å around 2.9 Å, as shown in Fig. 5(a). For consistency with previous works, we elected not to use the published potential here either. As a precaution, we reproduced the data corresponding to Fig. 1(a) of the main text with the published form. We performed five simulations per growth rate, and the comparison is shown in Fig. 5(b). Our results are not significantly affected by the change, a conclusion that is shared by other groups [16].

[1] M. J. Baldwin and R. P. Doerner, Nucl. Fusion **48**, 35001 (2008).
[2] S. Kajita, W. Sakaguchi, N. Ohno, N. Yoshida, and T. Saeki, Nucl. Fusion **49**, 95005 (2009).
[3] V. Borovikov, A. F. Voter, and X.-Z. Tang, J. Nucl. Mater. **254**, 447 (2014).

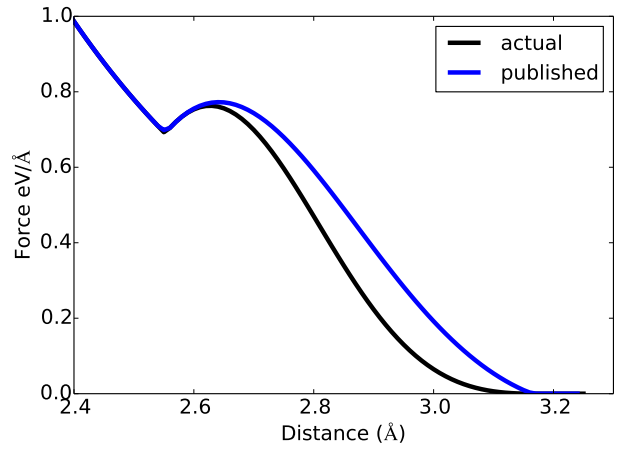

a)

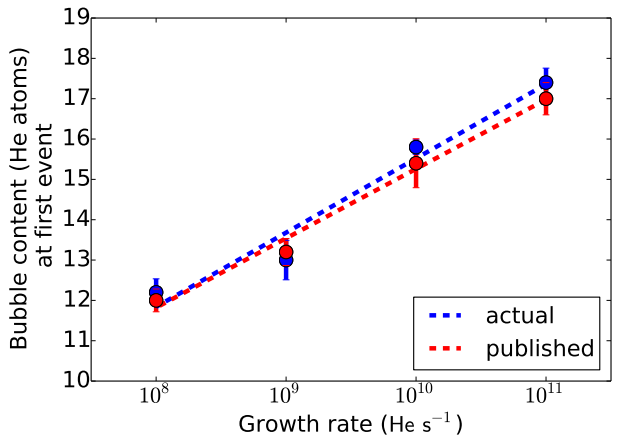

b)

FIG. 5. Comparison the between actual and published W-He potentials: a) W-He forces as a function of distance; b) Bubble content at the first detected event.

[4] F. Sefta, K. D. Hammond, N. Juslin, and B. D. Wirth, Nucl. Fusion **53**, 073015 (2013).

[5] G. De Temmerman, K. Bystrov, R. P. Doerner, L. Marot, G. M. Wright, K. B. Woller, and D. G. Whyte, J. Nucl. Mater. **438**, S78 (2013).

[6] C. H. Rycroft, G. S. Grest, J. W. Landry, and M. Z. Bazant, Phys. Rev. E **74**, 021306 (2006).

[7] "Visit," `https://wci.llnl.gov/codes/visit/home.html`.

[8] A. Stukowski, Modelling Simul. Mater. Sci. Eng. **18**, 015012 (2010).

[9] K. Nordlund, M. Ghaly, R. S. Averback, M. Caturla, T. Diaz de la Rubia, and J. Tarus, Phys. Rev. B **57**, 7556 (1998).

[10] L. Malerba, D. Terentyev, P. Olsson, R. Chakarova, and J. Wallenius, J. Nucl. Mater. **329-333**, 1156 (2004).

[11] A. F. Voter, F. Montalenti, and T. Germann, Annu. Rev. Mater. Res. **32**, 321 (2002).

[12] N. Juslin and B. D. Wirth, J. Nucl. Mater. **438**, S1221 (2013).

[13] F. Sefta, N. Juslin, and B. D. Wirth, J. Appl. Phys. **114**, 243518 (2013).

[14] F. Sefta, N. Juslin, K. D. Hammond, and B. D. Wirth, J. Nucl. Mater. **438**, S493 (2013).

[15] N. Juslin and B. D. Wirth, J. Nucl. Mater. **432**, 61 (2013).

[16] B. D. Wirth, Private communication.